

Article

# A Novel Non-Metallic Photocatalyst: Phosphorus-Doped Sulfur Quantum Dots

Ziyi Liu <sup>1</sup>, Chuanfu Shan <sup>1</sup>, Guiyu Wei <sup>1</sup>, Jianfeng Wen <sup>1</sup>, Li Jiang <sup>1</sup>, Guanghui Hu <sup>1</sup>, Zhijie Fang <sup>2</sup>,  
Tao Tang <sup>1,\*</sup> and Ming Li <sup>1,\*</sup>

<sup>1</sup> College of Science & Key Laboratory of Low-Dimensional Structural Physics and Application, Education Department of Guangxi Zhuang Autonomous Region, Guilin University of Technology, Guilin 541004, China

<sup>2</sup> School of Electronics Engineering, Guangxi University of Science and Technology, Liuzhou 545006, China

\* Correspondence: tangtao@glut.edu.cn (T.T.); liming928@163.com (M.L.)

**Abstract:** In this paper, a novel phosphorus-doped sulfur quantum dots (P-SQDs) material was prepared using a simple hydrothermal method. P-SQDs have a narrow particle size distribution as well as an excellent electron transfer rate and optical properties. Compositing P-SQDs with graphitic carbon nitride (g-C<sub>3</sub>N<sub>4</sub>) can be used for photocatalytic degradation of organic dyes under visible light. More active sites, a narrower band gap, and stronger photocurrent are obtained after introducing P-SQDs into g-C<sub>3</sub>N<sub>4</sub>, thus promoting its photocatalytic efficiency by as much as 3.9 times. The excellent photocatalytic activity and reusability of P-SQDs/g-C<sub>3</sub>N<sub>4</sub> are prospective signs of its photocatalytic application under visible light.

**Keywords:** phosphorus-doping; sulfur quantum dots; photocatalysis; charge transfer



**Citation:** Liu, Z.; Shan, C.; Wei, G.; Wen, J.; Jiang, L.; Hu, G.; Fang, Z.; Tang, T.; Li, M. A Novel Non-Metallic Photocatalyst: Phosphorus-Doped Sulfur Quantum Dots. *Molecules* **2023**, *28*, 3637. <https://doi.org/10.3390/molecules28083637>

Academic Editors: Guohui Dong, Na Chen, Wei Liu and Jingtao Bi

Received: 16 March 2023

Revised: 13 April 2023

Accepted: 17 April 2023

Published: 21 April 2023



**Copyright:** © 2023 by the authors. Licensee MDPI, Basel, Switzerland. This article is an open access article distributed under the terms and conditions of the Creative Commons Attribution (CC BY) license (<https://creativecommons.org/licenses/by/4.0/>).

## 1. Introduction

The energy crisis, environmental pollution, and climate change caused by excessive consumption of fossil energy have become the focus of global attention [1]. Currently, human demand for energy is increasing, and fossil energy extraction and use has brought about serious environmental pollution problems. Various organic dyes, chemicals, and other pollutants are discharged directly into the water, causing serious water pollution. Some conventional wastewater treatment methods are not effective in removing these widely available organic pollutants (e.g., dyes, antibiotics, pharmaceuticals). Therefore, how to effectively combat water pollution has become an important issue for researchers [2,3].

Photocatalysis is of great interest to researchers, because it can use natural solar energy as a driving force to achieve photocatalytic decomposition of water for hydrogen production and degradation of organic pollutants [4]. In the last decade, many photocatalysts have been investigated, such as biochar (BC) [5], graphitic phase carbon nitride (g-C<sub>3</sub>N<sub>4</sub>) [6], titanium dioxide (TiO<sub>2</sub>) [7,8], and various other new green and environmentally friendly materials. Among them, g-C<sub>3</sub>N<sub>4</sub> is widely used because it is superior in easy synthesis, unique electronic band structure and high physicochemical stability [9–14]. However, the small specific surface area, narrow visible light absorption range, and fast complexation of photogenerated electron-hole pairs seriously limit its practical application in photocatalysis. Therefore, compositing other materials with g-C<sub>3</sub>N<sub>4</sub> to improve the photogenerated carrier utilization efficiency has become one of the current research hotspots in the photocatalysis field [15]. Carbon-based quantum dots (CQDs), as one of the most well-known non-metallic elemental nanodots, have been widely used to composite with g-C<sub>3</sub>N<sub>4</sub> to form heterojunctions to substantially improve the photocatalytic efficiency [16–19], due to their excellent optical and electrical properties [20]. Interestingly, sulfur quantum dots (SQDs), another type of completely non-metallic nanodots, have attracted less attention in photocatalysis although they have similar optical properties to CQDs.

Elemental sulfur is one of the most abundant substances on Earth and has been widely used for centuries. In the last few years, SQDs, a new class of non-metallic fluorescent nanomaterials, have attracted great interest due to their unique optical, spectroscopic, chemical and antimicrobial properties [21,22]. In 2014, Li et al. demonstrated for the first time that zero-valent sulfur monomers can be prepared as fluorescent quantum dots and pointed out their potential for energy and photocatalytic applications [23]. At present, great progress has been made in the synthesis of SQDs. Shen et al. synthesized SQDs in one step and the prepared SQDs possess good stability and temperature responsiveness, and exhibit strong photocatalytic activity [24]. The SQDs were synthesized by Song et al. and possess advantages such as low cost, surface functionalization convenience, and unique photoluminescence (PL) properties, thus being able to be used as photosensitizers to broaden the light absorption range of  $g\text{-C}_3\text{N}_4$  and improving the photocatalytic activity of  $g\text{-C}_3\text{N}_4$  in visible light [25]. Cheng et al. reported that  $\alpha$ -sulfur crystals produce hydroxyl radicals ( $\cdot\text{OH}$ ) under light and have the ability to decompose RhB [26]. However, SQDs based on a single element S lack the adjustment methods to tune the physicochemical properties, thus limiting the further application in the photocatalytic field. Heteroatom doping is an effective way to tune the physical properties of experimental materials. Additionally, among the non-metal doping, sulfur-doped  $g\text{-C}_3\text{N}_4$  can change the electronic structure of  $g\text{-C}_3\text{N}_4$ , adjust the position of conduction band (CB) and valence band (VB), enhance the carrier mobility, and improve the photocatalytic activity. Phosphorus (P), a widely used dopant in carbon-based materials, has been proved to successfully modifying the physicochemical properties of GQDs, such as tuning the electronic structure, introducing surface functional groups and enhancing the electron transfer properties, thus significantly enhancing the photodegradation ability of organic dyes when compositing P-GQDs with  $g\text{-C}_3\text{N}_4$  [16]. P-doping is believed to have a similar modifying effect in SQDs.

In this work, phosphorus doping of SQDs and modification of  $g\text{-C}_3\text{N}_4$  were used via a hydrothermal method, and the prepared composites exhibited excellent photocatalytic degradation of colored dyes under visible light irradiation, being the first composite of hetero-element-doped SQDs for photocatalytic applications. This study provides experimental guidance for the design and synthesis of nanostructured photocatalysts in the future by elucidating their visible photocatalytic mechanism while expanding the applications of  $g\text{-C}_3\text{N}_4$ -based photocatalysts in the fields of pollutant degradation, solar cells, and artificial photosynthesis for hydrogen production.

## 2. Results and Discussion

### 2.1. Morphological Structure Characterization

The microstructural morphologies of the  $g\text{-C}_3\text{N}_4$  and P-SQDs/ $g\text{-C}_3\text{N}_4$  samples were investigated using TEM and SEM. We found that all these P-SQDs (Figure 1a) exhibit good uniform dispersion and high crystal structure with a spherical shape. The obtained P-SQDs show a uniform size distribution with an average diameter of 3 nm for P-SQDs (Figure 1b). In addition, the lattice spacing of P-SQDs was clearly shown to be 0.46 nm in HRTEM (Figure 1a, inset). The surface morphology and elemental composition of the synthesized photocatalysts were verified through SEM, respectively (Figure 1c–f). The pure  $g\text{-C}_3\text{N}_4$  (Figure 1c) shows an aggregated lamellar structure with an irregularly shaped graphite structure, which is typical of  $g\text{-C}_3\text{N}_4$  synthesized via polymerization methods [27]. SEM images of micron-scale P-SQDs/ $g\text{-C}_3\text{N}_4$  (Figure 1d,e) show that P-SQDs molecules are uniformly and tightly attached to the surface of  $g\text{-C}_3\text{N}_4$ . In Figure 1f, the distributions of P, S on P-SQDs/ $g\text{-C}_3\text{N}_4$  in the P-SQDs/ $g\text{-C}_3\text{N}_4$  composite are observed. It clearly shows the good distribution of P and S elements in P-SQDs/ $g\text{-C}_3\text{N}_4$ . These results strongly demonstrate the uniform distribution of P-SQDs and the successful composition of  $g\text{-C}_3\text{N}_4$  with P-SQDs. In Figure 1d,e, the cohesive lamellar structure of P-SQDs/ $g\text{-C}_3\text{N}_4$  shows many bends, folds, and overlapping layers, and the unique structure facilitates the migration of charge carriers and the diffusion of substances in an aqueous solution. This would be beneficial as regards improving the activity of photocatalytic reactions.

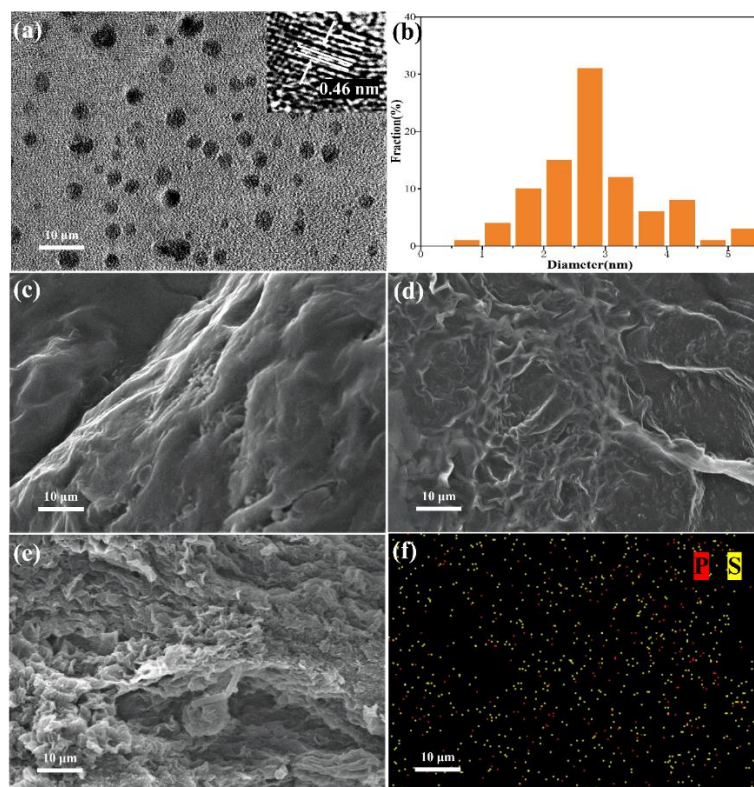


**Figure 1.** (a) TEM image of P-SQDs, the inset is a HRTEM image of P-SQDs showing the lattice spacing, (b) particle size distribution of P-SQDs. SEM images of (c)  $g\text{-C}_3\text{N}_4$  and (d,e) P-SQDs/ $g\text{-C}_3\text{N}_4$ , (f) the EDS elemental map image of P-SQDs/ $g\text{-C}_3\text{N}_4$ .

The specific surface area and pore structure of  $g\text{-C}_3\text{N}_4$  and P-SQDs/ $g\text{-C}_3\text{N}_4$  photocatalysts were investigated via nitrogen adsorption–desorption analysis, and the results are shown in Figure 2. The specific surface area and pore size of P-SQDs/ $g\text{-C}_3\text{N}_4$  composites are superior to those of pure  $g\text{-C}_3\text{N}_4$ . In Figure 2a, it can be seen that both  $g\text{-C}_3\text{N}_4$  and P-SQDs/ $g\text{-C}_3\text{N}_4$  are type IV isotherms with hysteresis loops. The increase in specific surface area of P-SQDs/ $g\text{-C}_3\text{N}_4$  is due to the increase in pore volume in the diameter range of 2–30 nm (Figure 2b), corresponding to the accumulation of broken small particles due to partial polymerization [28]. P-SQDs/ $g\text{-C}_3\text{N}_4$  exhibits the largest pore volume in the range of 2–5 nm in diameter [29]. It was demonstrated that by modifying  $g\text{-C}_3\text{N}_4$  with P-SQDs, not only can the specific surface area be increased, but the pore size can also be increased to make them richer in active sites, which is conducive to improving the adsorption capacity of the composites on dye wastewater.

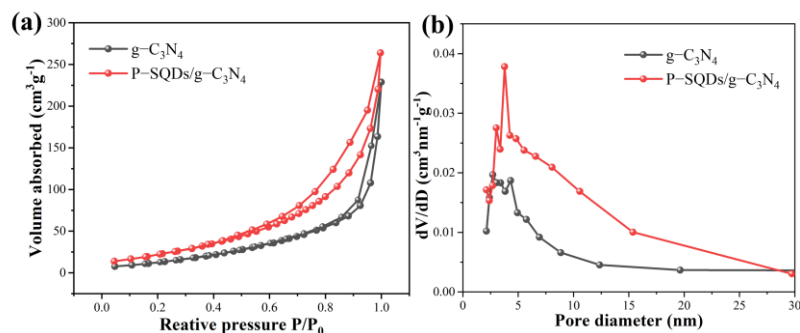


**Figure 2.** (a)  $\text{N}_2$  adsorption–desorption isotherms and (b) pore size distribution curves of  $g\text{-C}_3\text{N}_4$  and P-SQDs/ $g\text{-C}_3\text{N}_4$ .

## 2.2. Nanostructure Investigation

XRD is commonly used to determine the crystal structure of the material (Figure 3a). In the XRD pattern of  $g\text{-C}_3\text{N}_4$ , two distinct diffraction peaks were observed. The peak at  $13.1^\circ$  indicates that the (100) crystal plane produces tri-s-triazine units, while the other peak at  $27.3^\circ$  is attributed to the interlayer stacking of aromatic segments in the (002) crystal plane (PDF#87-1526). These two diffraction peaks are in good agreement with the previously reported  $g\text{-C}_3\text{N}_4$  [30–32]. Notably, P-SQDs/ $g\text{-C}_3\text{N}_4$  shows a diffraction peak different from that of  $g\text{-C}_3\text{N}_4$ , a new peak located at  $10.6^\circ$  ( $d = 0.83$  nm). This peak, reported by other articles, is related to the hydrolysis/oxidation of  $g\text{-C}_3\text{N}_4$ , which reduces the polymerization of  $g\text{-C}_3\text{N}_4$  and promotes the formation of  $g\text{-C}_3\text{N}_4$  containing oxygen functional groups [31,33,34]. During the hydrothermal treatment, the alignment of the tri-s-triazine units changes due to the hydrolysis/oxidation process. The peak at  $27.6^\circ$  corresponds to the interlayer stacking of the aromatic segments at a distance of 0.32 nm. The XRD peak in Figure 3a shifts from  $27.3^\circ$  for  $g\text{-C}_3\text{N}_4$  to  $27.6^\circ$  for P-SQDs/ $g\text{-C}_3\text{N}_4$ , and the interlayer distance also decreased from 0.326 nm to 0.322 nm accordingly. It is also observed that the characteristic peaks of P-SQDs/ $g\text{-C}_3\text{N}_4$  are much more pronounced than those of  $g\text{-C}_3\text{N}_4$ , implying a higher degree of  $\pi$ -electron conjugation. In addition, the ratio of  $27.6^\circ$  to  $10.6^\circ$  peaks in P-SQDs/ $g\text{-C}_3\text{N}_4$  is greater than 1, further indicating the formation of higher-order  $\pi$ - $\pi$  stacking in P-SQDs/ $g\text{-C}_3\text{N}_4$  [35–37]. XRD images show that P-SQDs/ $g\text{-C}_3\text{N}_4$  has good crystallinity, while the diffraction peaks of the composite material are enhanced and long-range ordering was improved.

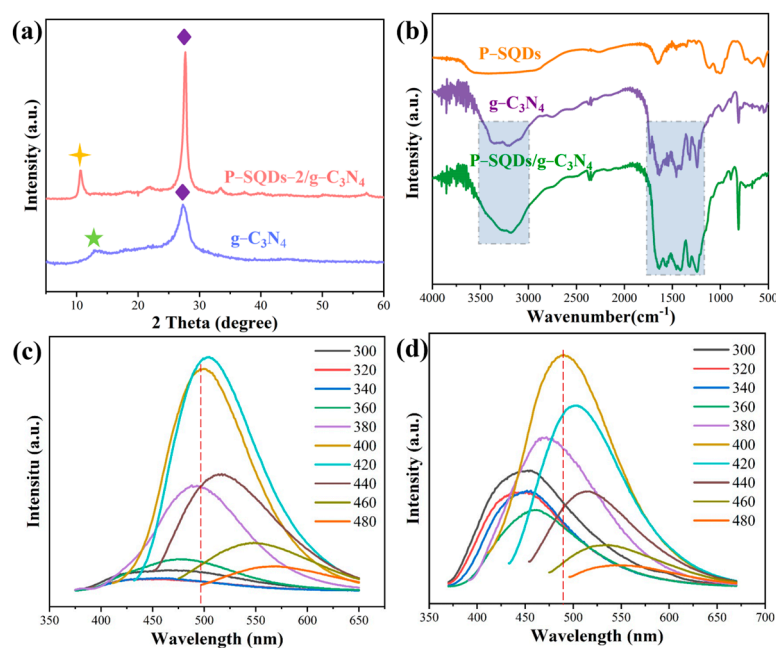


**Figure 3.** (a) XRD patterns of  $g\text{-C}_3\text{N}_4$  and P-SQDs/ $g\text{-C}_3\text{N}_4$ . (b) FTIR images of P-SQDs,  $g\text{-C}_3\text{N}_4$ , and P-SQDs/ $g\text{-C}_3\text{N}_4$ . PL spectra of (c) SQDs and (d) P-SQDs at different excitation wavelengths.

FTIR spectra are shown in Figure 3b. The broad signal of P-SQDs at  $1097\text{ cm}^{-1}$  is caused by the stretching vibration of C-O-H or C-O-C [24]. The C-C bending vibration peak ( $1097\text{ cm}^{-1}$ ) in P-SQDs/ $g\text{-C}_3\text{N}_4$  composites is not significant compared to P-SQDs, which may be due to the C-C bond breakage in P-SQDs [35]. The absorption peak at  $814\text{ cm}^{-1}$ , which is present in both pure  $g\text{-C}_3\text{N}_4$  and P-SQDs/ $g\text{-C}_3\text{N}_4$ , is attributed to the tri-s-triazine unit [38]. The peaks at  $1200\text{--}1600\text{ cm}^{-1}$  are the stretching vibrations of the aromatic C-N groups [39], while the  $3000\text{--}3500\text{ cm}^{-1}$  broad absorption peaks are caused by the stretching vibrations of N-H and -OH [17]. Based on the positions of the characteristic peaks of P-SQDs/ $g\text{-C}_3\text{N}_4$ , it can be seen that the addition of P-SQDs did not change the structure of  $g\text{-C}_3\text{N}_4$ . Additionally, the intensities of these characteristic peaks in P-SQDs/ $g\text{-C}_3\text{N}_4$

are even higher than those of pure  $g\text{-C}_3\text{N}_4$ , indicating that more tri-s-triazine units and aromatic C-N heterocycles were formed while the C-C bonds were broken in the biochar. More tri-s-triazine units and aromatic heterocycles can induce stronger  $\pi\text{-}\pi$  interactions in the P-SQDs/ $g\text{-C}_3\text{N}_4$  composites, which facilitates the electron delocalization effect and further promotes electron transport in the photocatalytic process.

We investigated the optical properties of the synthesized P-SQDs and SQDs (Figure 3c,d). P-SQDs have a maximum emission intensity of 490 nm under a 400 nm excitation, while SQDs show maximum emission intensity of 505 nm at a 420 nm excitation. As the excitation wavelength increased from 300 to 480 nm, the emission wavelength of P-SQDs gradually red-shifted from 445 to 542 nm, indicating the occurrence of photon reabsorption. The emissive intensities are also excitation-dependent, coming up with a decrease–increase–decrease tendency. In addition, Figure 3c,d shows that at the same excitation wavelength (400 nm), the PL of P-SQDs undergoes a significant red shift compared to SQDs. It is mainly due to the increased conjugation of phosphorus elements after doping.

The chemical composition of P-SQDs was further characterized through XPS. As seen in Figure 4a, elements of C, O, S, and P were found in P-SQDs. It can be seen from the spectrum that 284.8, 531.3, 230.9, 165.3, 188.3 and 132.5 eV were attributed to C 1s, O 1s, S 2s, S 2p, P 2s, and P 2p, respectively. In Figure 4b, there are four major peaks at 287.4 eV (C=O), 285 eV (C–P), 284.8 eV (C–C), 283.4 eV (C=C), on the C 1s spectrum of P-SQDs [40]. The S 2p spectra of P-SQDs (Figure 4c) show five sulfur species exhibited in the reaction mixture, including  $\text{SO}_4^{2-}$  (168.4 eV),  $\text{SO}_3^{2-}$  (167.2 eV), C–S (165.5 eV),  $\text{S}_x^{2-}$  (162.4 eV), and divalent sulfur ions ( $\text{S}^{2-}$  and  $\text{S}_x^{2-}$ ) (161.5 eV), respectively [20,26]. Two peaks at 133.4 and 134.2 eV show the P 2p spectra (Figure 4d), which confirmed the presence of P–C and P–O bonds [41].

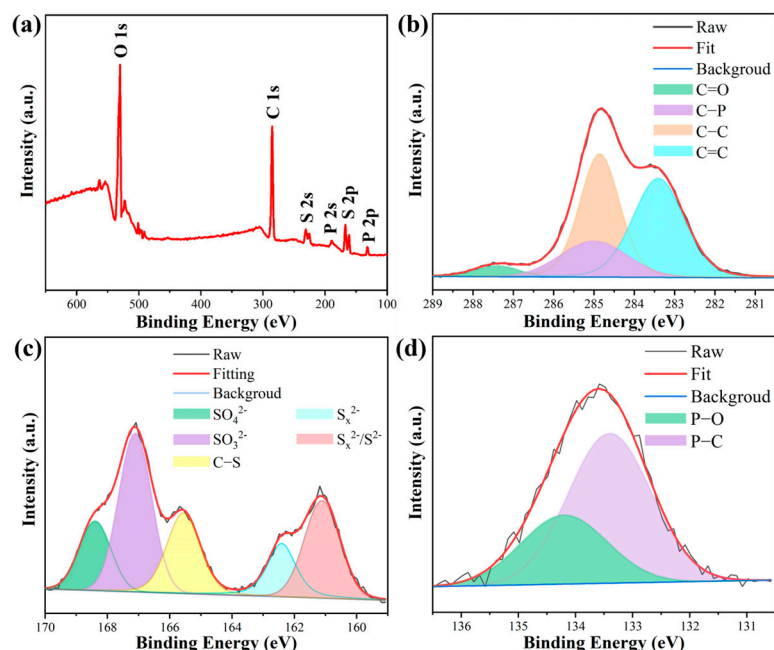


**Figure 4.** (a) XPS survey of P-SQDs. The corresponding high-resolution XPS spectra for (b) C 1s, (c) S 2p and (d) P 2p.

### 2.3. Band Structure and Photoelectric Properties

The UV–vis absorption spectra of P-SQDs/ $g\text{-C}_3\text{N}_4$  and  $g\text{-C}_3\text{N}_4$  are shown in Figure 5a. Pure  $g\text{-C}_3\text{N}_4$  has a clear absorption edge at about 450 nm [42]. When P-SQDs are complexed onto  $g\text{-C}_3\text{N}_4$ , the absorption band redshifts at about 465 nm, indicating a higher band to band absorption ability of visible light. According to Tauc method, the band gaps of P-SQDs/ $g\text{-C}_3\text{N}_4$  and  $g\text{-C}_3\text{N}_4$  are 2.96 and 3.00 eV, respectively (inset of Figure 5a). At the

same time, the absorbance of P-SQDs/g-C<sub>3</sub>N<sub>4</sub> in the visible range (465 nm to 800 nm) is increased by a factor of 2.78, also representing a better absorption in visible light [43].

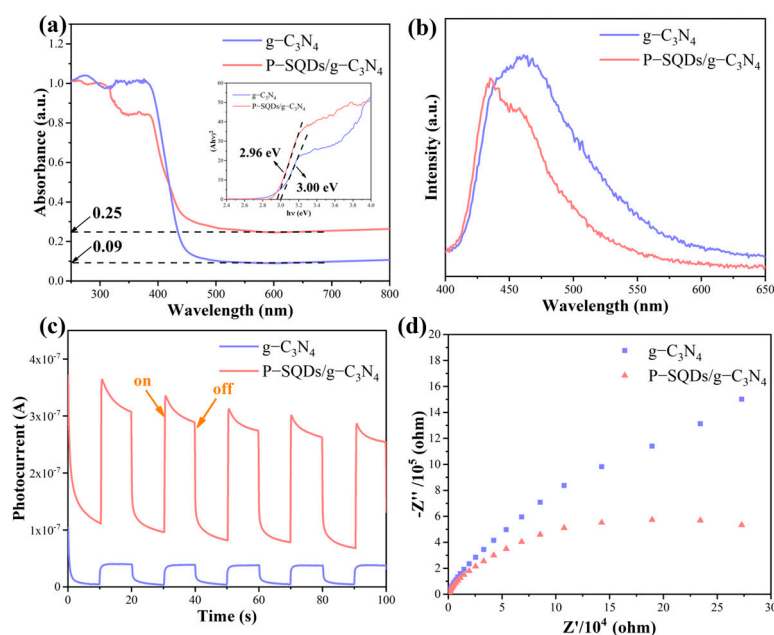


**Figure 5.** The comparison of P-SQDs/g-C<sub>3</sub>N<sub>4</sub> and g-C<sub>3</sub>N<sub>4</sub>. (a) UV-vis absorption spectra (the insert are band gap simulations using Tauc function). (b) Steady-state PL spectra. (c) Transient photocurrent curves. (d) EIS.

To investigate the separation and transfer of photogenerated carriers in P-SQDs/g-C<sub>3</sub>N<sub>4</sub>, we further conducted PL, TPR, and EIS measurements. Figure 5b shows the PL spectra under the excitation wavelength of 345 nm. A strong photocarrier recombination of g-C<sub>3</sub>N<sub>4</sub> is exhibited with an emissive peak centered at 460 nm. The PL spectra of P-SQDs/g-C<sub>3</sub>N<sub>4</sub> show a slight blue shift of 25 nm compared to g-C<sub>3</sub>N<sub>4</sub>, which is attributed to the quantum confinement effects [44]. In contrast, the emission intensity of P-SQDs/g-C<sub>3</sub>N<sub>4</sub> is significantly lower than that of g-C<sub>3</sub>N<sub>4</sub>, which indicates that P-SQDs/g-C<sub>3</sub>N<sub>4</sub> has a lower direct recombination efficiency of the photogenerated electron-hole (e-h) pairs. The transient photocurrent curves (Figure 5c) reveal that the lower e-h direct recombination ratio comes from the charge separation and transfer. Under the white light of a 300 W xenon lamp, the photocurrent response of P-SQDs/g-C<sub>3</sub>N<sub>4</sub> is significantly enhanced compared to that of g-C<sub>3</sub>N<sub>4</sub>, indicating a fast and reversible photocurrent response, which means that in P-SQDs/g-C<sub>3</sub>N<sub>4</sub>, more photogenerated carriers can participate in current conduction while not directly recombining to emit PL. Namely, the charge separation and transfer in P-SQDs/g-C<sub>3</sub>N<sub>4</sub> are more effective. At the same time, EIS analyses were performed and are shown in Figure 5d. P-SQDs/g-C<sub>3</sub>N<sub>4</sub> exhibits a smaller arc radius, also demonstrating a higher charge separation and transfer efficiency [45]. Combined with the above experimental results, the compounding of P-SQDs with g-C<sub>3</sub>N<sub>4</sub> leads to an increase in visible light utilization and improves the separation and transfer efficiency of photogenerated carriers, which favors a better photocatalytic performance.

#### 2.4. Photocatalytic Performance

The photocatalytic performances of g-C<sub>3</sub>N<sub>4</sub>, P-SQDs, SQDs/g-C<sub>3</sub>N<sub>4</sub>, P-SQDs-1/g-C<sub>3</sub>N<sub>4</sub>, P-SQDs-2/g-C<sub>3</sub>N<sub>4</sub>, and P-SQDs-3/g-C<sub>3</sub>N<sub>4</sub> were tested with a 300 W Xe lamp, respectively (Figure 6a). Under the same experimental conditions, after 120 min, MO itself hardly degraded under white light, and g-C<sub>3</sub>N<sub>4</sub> can only photodegrade 63.36% MO, while P-SQDs-2/g-C<sub>3</sub>N<sub>4</sub> showed excellent photocatalytic degradation efficiency, 98.72%. Notably, SQDs showed no observable photodegradation ability in our experiments. The

MO degradation rates of P-SQDs-1/g-C<sub>3</sub>N<sub>4</sub>, P-SQDs-2/g-C<sub>3</sub>N<sub>4</sub>, and P-SQDs-3/g-C<sub>3</sub>N<sub>4</sub> were 87.35%, 98.72%, and 34.69%, respectively. Too much P-SQDs addition leads to a decrease in the photocatalytic activity, it may be attributed to the fact that excessive P-SQDs would block the effective light contact area of g-C<sub>3</sub>N<sub>4</sub>. This situation is also observed in graphene quantum dots and carbon nitride composites [17]. The kinetic behavior was described using the first-order kinetic equation [ $\ln(C_t/C_0) = kt$ , where  $k$  is the reaction rate constant,  $C_t$  is the MO concentration at reaction time  $t$ , and  $C_0$  is the initial MO concentration]. The value of  $k$  of P-SQDs-2/g-C<sub>3</sub>N<sub>4</sub> was 3.9 times higher than that of g-C<sub>3</sub>N<sub>4</sub> (Figure 6b). From the perspective of practical application, the stability and durability of photocatalysts are also important. To confirm the stability and durability of P-SQDs/g-C<sub>3</sub>N<sub>4</sub>, repeated experiments were performed under the same experimental conditions (Figure 6c), and it can be seen that the catalytic efficiency of P-SQDs-2/g-C<sub>3</sub>N<sub>4</sub> remained unchanged after three repetitions. Figure 6d shows the variation of the MO absorption peak after P-SQDs/g-C<sub>3</sub>N<sub>4</sub> photodegradation, and the decrease in its absorption ability and the blueshift of the peak indicates that MO was decomposed and its structure also changed.

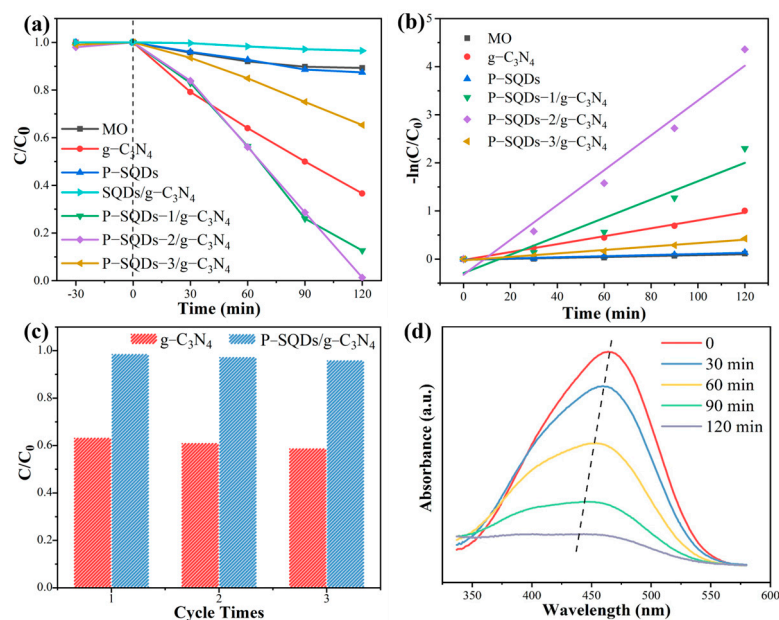


**Figure 6.** (a) Effect of different samples on the photocatalytic degradation of MO under visible light (Xe lamp). (b) The corresponding degradation kinetic behavior. (c) The photocatalytic cycle tests of g-C<sub>3</sub>N<sub>4</sub> and P-SQDs/g-C<sub>3</sub>N<sub>4</sub>. (d) UV-vis spectra of MO solution after P-SQDs/g-C<sub>3</sub>N<sub>4</sub> degradation with time.

### 2.5. Analysis of the Photocatalytic Mechanism

In order to have a deeper understanding of the roles of the active components in the photocatalytic process, P-benzoquinone (p-BQ), potassium dichromate (K<sub>2</sub>Cr<sub>2</sub>O<sub>7</sub>), isopropanol (IPA), and potassium iodide (KI) were added as scavengers for the sudden inhibition of superoxide radicals ( $\cdot\text{O}_2^-$ ), electrons ( $e^-$ ), hydroxyl radicals ( $\cdot\text{OH}$ ), and holes ( $h^+$ ), respectively. As shown in Figure 7, without the addition of scavengers, the reaction system was essentially completely degraded, indicating that no free radicals were hindered. While the degradation rate of the reaction system with the addition of p-BQ and KI was inhibited, which indicates that the  $\cdot\text{O}_2^-$  and  $h^+$  radicals in the catalyst play a crucial role in the photocatalytic process. The degradation rate of the reaction system with the addition of K<sub>2</sub>Cr<sub>2</sub>O<sub>7</sub> was also reduced, indicating that  $e^-$  is also one of the active substances for the photocatalytic degradation of P-SQDs/g-C<sub>3</sub>N<sub>4</sub>. The effects of the active substances were ranked as  $\cdot\text{O}_2^- > h^+ > e^-$ .

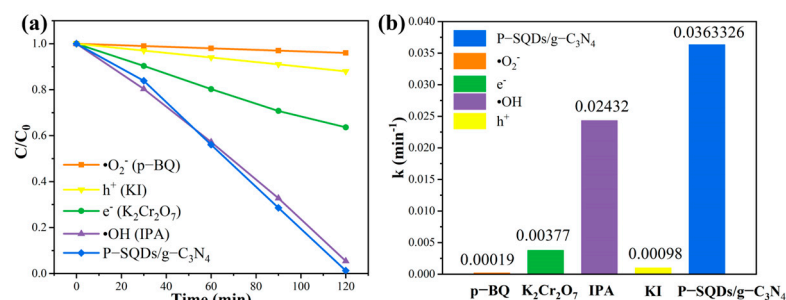


**Figure 7.** (a) Effect of scavengers on the catalytic effect of P-SQD/g- $\text{C}_3\text{N}_4$ . (b) The reaction rate of P-SQD/g- $\text{C}_3\text{N}_4$  in trapping experiments under visible light irradiation.

According to the Mott–Schottky curves in Figure 8a,b, it is known that the conduction band minimum (CBM) of P-SQDs/g- $\text{C}_3\text{N}_4$  is  $-0.55$  eV, and a bit higher than g- $\text{C}_3\text{N}_4$  ( $-0.57$  eV). Combined with the band gap analyses (Figure 5a), we give the band structures of these samples. Thus, a possible mechanism for the photocatalytic degradation of P-SQDs/g- $\text{C}_3\text{N}_4$  was developed. As shown in Figure 8, g- $\text{C}_3\text{N}_4$  can absorb a part of visible light; therefore, photogenerated electrons are excited from the valence to the conduction band under the visible light. The forementioned TPR and EIS results have shown that P-SQDs can promote the separation of the photogenerated e–h pairs in g- $\text{C}_3\text{N}_4$  to suppress their direct recombination; thus,  $\text{O}_2$  is converted to  $\cdot\text{O}_2^-$  by the photogenerated electrons, while water is decomposed to OH by the holes. MO is oxidized to  $\text{CO}_2$  and  $\text{H}_2\text{O}$  by the active groups. Moreover, compared to g- $\text{C}_3\text{N}_4$ , the enhancement of visible light absorption due to the narrower band gap of P-SQDs/g- $\text{C}_3\text{N}_4$  (Figure 5a), will further improve the photocatalytic performance and decompose MO in a shorter time.

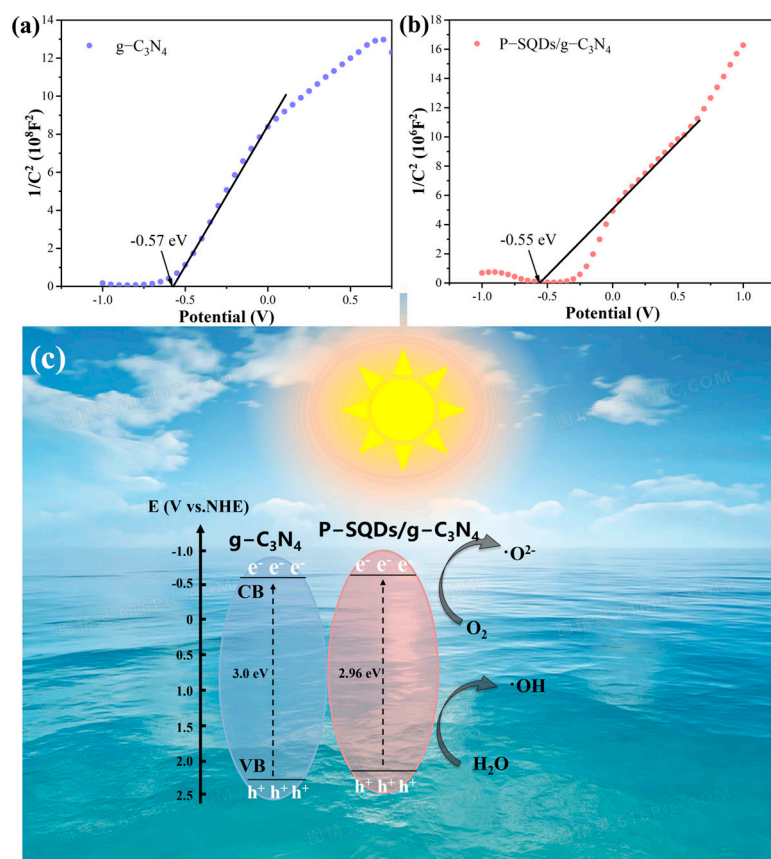


**Figure 8.** Mott-Schottky curves of (a) g- $\text{C}_3\text{N}_4$  and (b) P-SQDs/g- $\text{C}_3\text{N}_4$ . (c) Schematic diagram of photocatalytic mechanism of the P-SQDs/g- $\text{C}_3\text{N}_4$  under visible light irradiation.

### 3. Experimental Section

#### 3.1. Material

Sulfur Sublimed (S,  $\geq 99.5\%$ ) was purchased from Chengdu Kolon Chemical Co., Ltd. (Chengdu, China). Polyethylene glycol (PEG, Mn = 400 Da), sodium hydroxide (NaOH,  $\geq 96.0\%$ ), disodium hydrogen phosphate dodecahydrate ( $\text{Na}_2\text{HPO}_4 \cdot 12\text{H}_2\text{O}$ ,  $\geq 99.0\%$ ), urea ( $\text{H}_2\text{NCONH}_2$ ,  $\geq 99.0\%$ ), and methyl orange (MO) were purchased from Xilong Science Co., Ltd. (Shantou, China). All the raw materials were of analytical grade and used without further purification. The experimental water was deionized.

#### 3.2. Preparation of P-SQDs

We prepared P-SQDs using a hydrothermal method. SQDs were synthesized according to a previously reported procedure [25], as follows: 1.6 g S, 3 g PEG, 4 g NaOH, and 100 mL deionized water were stirred at  $90^\circ\text{C}$  for 10 h. After cooling to room temperature, impurities were removed with a  $0.22\ \mu\text{m}$  microporous membrane. Next, 1.2 g  $\text{Na}_2\text{HPO}_4$  was dissolved in 30 mL SQDs and treated with ultrasonication (500 W, 40 kHz) for 30 min, and then put into a Teflon autoclave and heated at  $180^\circ\text{C}$  for 10 h. After cooling to room temperature, it was dialyzed, and finally freeze-dried to obtain P-SQDs.

#### 3.3. Preparation of P-SQDs/g- $\text{C}_3\text{N}_4$

The g- $\text{C}_3\text{N}_4$  material was prepared by a thermal polycondensation method [17]: Putting 25 g urea into a crucible with a lid, and heating it in a muffle furnace at a rate of  $2.5^\circ\text{C}/\text{min}$  until  $550^\circ\text{C}$  to hold for 3 h, and then naturally cooling it to room temperature.

The P-SQD/g- $\text{C}_3\text{N}_4$  photocatalyst was prepared using a simple hydrothermal method. Firstly, 0.6 g g- $\text{C}_3\text{N}_4$  with X g P-SQD (X = 0.2, 0.4, 0.6) separately was dissolved in 80 mL water, after 30 min sonication, and then put into a Teflon autoclave, heated at  $180^\circ\text{C}$  for 6 h and cooled to room temperature. After centrifugal cleaning for three times and freeze-drying, the final products were obtained and named P-SQD-1/g- $\text{C}_3\text{N}_4$ , P-SQD-2/g- $\text{C}_3\text{N}_4$ , and P-SQD-3/g- $\text{C}_3\text{N}_4$ , respectively. Figure 9 briefly illustrates the experimental procedure of this study.

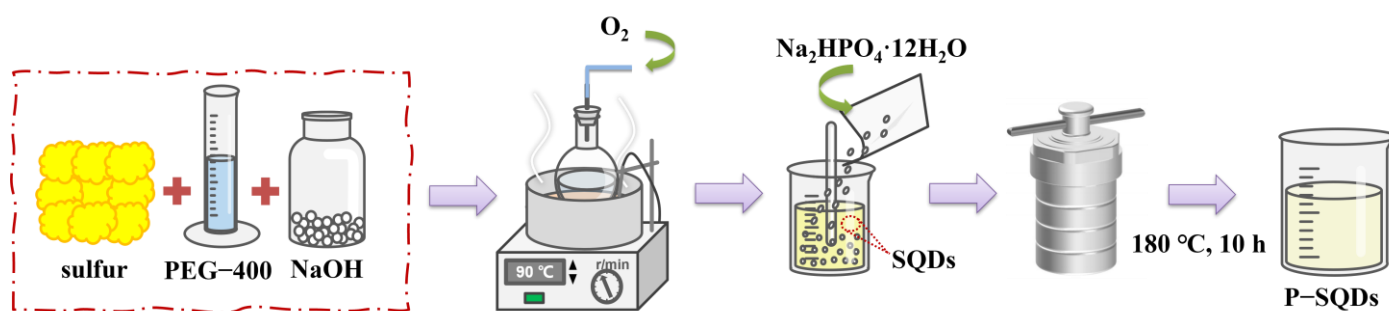


Figure 9. Preparation process scheme of P-SQDs/g- $\text{C}_3\text{N}_4$ .

#### 3.4. Characterization

The ultraviolet-visible (UV-vis) absorption spectra were recorded using a PerkinElmer Lambda 750 spectrophotometer (CT, Houston, TX, USA). The Fourier transform infrared (FTIR) spectra were measured with a NICOLET-6700 FTIR spectrometer (Tokyo, Japan). The crystal structure of the samples was studied by MiniFlex-600 (JEOL, Japan) X-ray diffractometer (XRD). Transmission electron microscopy (TEM, JEM-2100F (Tokyo, Japan)), scanning electron microscopy (SEM, KYKY-EM6900) and X-ray energy dispersive spectrometry (EDS, S-00123, USA) were used to study the particle size, morphology and elemental composition of the samples. The specific surface area was calculated by applying the Brunauer–Emmett–Teller (BET, JW-BK112) model to the adsorption data. The valence distribution and bonding patterns of the sample elements were measured by an ESCALAB-250XI (Waltham, MA, USA) X-ray photoelectron spectrometer. Photoluminescence (PL) spectra

were measured on a fluorescence spectrophotometer (Edinburgh FL/FS900 Carry Eclipse, Cheadle, UK). All the measurements were conducted at room temperature.

### 3.5. Electrochemical Measurements

The transient photocurrent response spectra (TPR), Mott–Schottky curves and electrochemical impedance spectra (EIS) Nyquist plots were performed with an electrochemical workstation (CHI 760E, Shanghai, China) under a standard three-electrode system (Pt-counter electrode, saturated glyceryl electrode-reference electrode, sample/FTO-working electrode). Na<sub>2</sub>SO<sub>4</sub> solution (0.5 M) was used as the electrolyte and a 300 W xenon lamp was used as the light source to measure the photocurrent response. The synthesized photocatalyst was deposited on the electrode using the following method: 0.01 g of the sample was dispersed into ethanol to form a suspension, and then, the formed homogeneous suspension was transferred to the FTO glass electrode. Finally, the prepared electrode was dried at 70 °C for 12 h.

### 3.6. Photocatalytic Degradation Experiments

Methyl orange (MO) solution was chosen to simulate the pollutants to study the photocatalytic properties of the samples. The experiments were conducted at room temperature as a whole. Separately, 50 mg of samples were placed into 50 mL of MO solution (10 mg/L) and firstly stirred in a dark environment for 30 min to ensure that the catalyst reached adsorption–desorption equilibrium with the pollutant. Then, the samples were irradiated under a xenon lamp (300 W), and 3 mL of the reaction solution was taken every 30 min and filtered through a 0.22 µm polyethersulfone (PES) needle filter to remove the suspended catalyst. Finally, the MO concentration at 463 nm was measured using UV–vis spectrophotometers.

## 4. Conclusions

In summary, excitation-dependent fluorescent P-SQDs with ultra-small size and narrow size distribution were synthesized for the first time at ambient conditions. Complexes of P-SQDs with g-C<sub>3</sub>N<sub>4</sub> were obtained using a simple hydrothermal synthesis strategy, and P-SQDs/g-C<sub>3</sub>N<sub>4</sub> exhibited good and stable photocatalytic effects. Its MO photodegradation rate was as high as 98.72%, much higher than that of pure g-C<sub>3</sub>N<sub>4</sub>, and it also exhibited good cycling stability. An increase in the specific surface area of the photocatalytic material, a decrease in the band gap width, an increase in the separation efficiency of photogenerated electron–hole pairs, and an enhancement and expansion of visible light absorption were achieved, resulting in significant photocatalytic activity and kinetics. We highlight that a novel metal-free quantum dot was developed and it can be used as an efficient photocatalyst. This work not only shows the great potential of P-SQDs/g-C<sub>3</sub>N<sub>4</sub> as a photocatalyst, but also reveals a multi-layered structure for dramatically enhancing the photocatalytic activity by adding non-metallic material quantum dots.

**Author Contributions:** Conceptualization, Z.L.; methodology, C.S. and M.L.; software, G.W.; validation, T.T.; formal analysis, J.W. and Z.F.; investigation, M.L. and L.J.; resources, M.L.; data curation, Z.L.; writing—original draft preparation, Z.L.; writing—review and editing, T.T., G.H. and M.L.; visualization, Z.L. and T.T.; supervision, M.L.; project administration, M.L.; funding acquisition, M.L., L.J. and G.H. All authors have read and agreed to the published version of the manuscript.

**Funding:** This work was financially supported by the National Natural Science Foundation of China (12164013), the Natural Science Foundation of Guangxi Province (2020GXNSFBA297125), the Science and Technology Base and Talent Special Project of Guangxi Province (AD21220029), and innovation Project of Guangxi Graduate Education (YCSW2022331).

**Institutional Review Board Statement:** Not applicable.

**Informed Consent Statement:** Not applicable.

**Data Availability Statement:** The data can be made available upon reasonable request.

**Conflicts of Interest:** The authors declare no conflict of interest.

**Sample Availability:** Not applicable.

## References

1. Low, J.X.; Yu, J.G.; Jaroniec, M.; Wageh, S.; Al-Ghamdi, A.A. Heterojunction photocatalysts. *Adv. Mater.* **2017**, *29*, 20. [[CrossRef](#)]
2. Cai, M.; Bai, D.; Li, H. Optimal planning of water pollution control. *J. Exp. Bot.* **2003**, *54*, 61.
3. Zhou, Z.; Liu, J.; Zhou, N.; Zhang, T.; Zeng, H. Does the “10-point water plan” reduce the intensity of industrial water pollution? Quasi-experimental evidence from China. *J. Environ. Manag.* **2021**, *295*, 113048. [[CrossRef](#)]
4. Wageh, S.; Al-Ghamdi, A.A.; Jafer, R.; Li, X.; Zhang, P. A new heterojunction in photocatalysis: S-scheme heterojunction. *Chin. J. Catal.* **2021**, *42*, 667–669. [[CrossRef](#)]
5. Yang, B.; Dai, J.; Zhao, Y.; Wu, J.; Ji, C.; Zhang, Y. Advances in preparation, application in contaminant removal, and environmental risks of biochar-based catalysts: A review. *Biochar* **2022**, *4*, 51. [[CrossRef](#)]
6. Lin, H.; Wu, J.; Zhou, F.; Zhao, X.; Lu, P.; Sun, G.; Song, Y.; Li, Y.; Liu, X.; Dai, H. Graphitic carbon nitride-based photocatalysts in the applications of environmental catalysis. *J. Environ. Sci.* **2023**, *124*, 570–590. [[CrossRef](#)]
7. Belessiotis, G.V.; Falara, P.P.; Ibrahim, I.; Kontos, A.G. Magnetic metal oxide-based photocatalysts with integrated silver for water treatment. *Materials* **2022**, *15*, 4629. [[CrossRef](#)]
8. Ibrahim, I.; Belessiotis, G.V.; Elseman, A.M.; Mohamed, M.M.; Ren, Y.; Salama, T.M.; Mohamed, M.B.I. Magnetic TiO<sub>2</sub>/CoFe<sub>2</sub>O<sub>4</sub> photocatalysts for degradation of organic dyes and pharmaceuticals without oxidants. *Nanomaterials* **2022**, *12*, 3290. [[CrossRef](#)]
9. Ong, W.J.; Tan, L.L.; Ng, Y.H.; Yong, S.T.; Chai, S.P. Graphitic carbon nitride (g-C<sub>3</sub>N<sub>4</sub>)-based photocatalysts for artificial photosynthesis and environmental remediation: Are we a step closer to achieving sustainability? *Chem. Rev.* **2016**, *116*, 7159–7329. [[CrossRef](#)]
10. Yang, Y.; Zeng, G.; Huang, D.; Zhang, C.; He, D.; Zhou, C.; Wang, W.; Xiong, W.; Song, B.; Yi, H.; et al. In situ grown single-atom cobalt on polymeric carbon nitride with bidentate ligand for efficient photocatalytic degradation of refractory antibiotics. *Small* **2020**, *16*, 2001634. [[CrossRef](#)]
11. Zhang, P.; Tong, Y.; Liu, Y.; Vequizo, J.J.M.; Sun, H.; Yang, C.; Yamakata, A.; Fan, F.; Lin, W.; Wang, X.; et al. Heteroatom dopants promote two-electron O<sub>2</sub> reduction for photocatalytic production of H<sub>2</sub>O<sub>2</sub> on polymeric carbon nitride. *Angew. Chem. Int. Ed.* **2020**, *59*, 16209–16217. [[CrossRef](#)] [[PubMed](#)]
12. An, S.; Zhang, G.; Li, K.; Huang, Z.; Wang, X.; Guo, Y.; Hou, J.; Song, C.; Guo, X. Self-Supporting 3D carbon nitride with tunable n → pi\* electronic transition for enhanced solar hydrogen production. *Adv. Mater.* **2021**, *33*, 2104361. [[CrossRef](#)]
13. Liu, C.; Zhang, Y.; Dong, F.; Reshak, A.H.; Ye, L.; Pinna, N.; Zeng, C.; Zhang, T.; Huang, H. Chlorine intercalation in graphitic carbon nitride for efficient photocatalysis. *Appl. Catal. B* **2017**, *203*, 465–474. [[CrossRef](#)]
14. Hu, C.; Chen, F.; Wang, Y.; Tian, N.; Ma, T.; Zhang, Y.; Huang, H. Exceptional cocatalyst-free photo-enhanced piezocatalytic hydrogen evolution of carbon nitride nanosheets from strong in-plane polarization. *Adv. Mater.* **2021**, *33*, 2101751. [[CrossRef](#)]
15. Cao, S.W.; Low, J.X.; Yu, J.G.; Jaroniec, M. Polymeric photocatalysts based on graphitic carbon nitride. *Adv. Mater.* **2015**, *27*, 2150–2176. [[CrossRef](#)]
16. Guo, Z.; Wu, H.; Li, M.; Tang, T.; Wen, J.; Li, X. Phosphorus-doped graphene quantum dots loaded on TiO<sub>2</sub> for enhanced photodegradation. *Appl. Surf. Sci.* **2020**, *526*, 146724. [[CrossRef](#)]
17. Guo, Z.S.; Ni, S.N.; Wu, H.; Wen, J.F.; Li, X.Y.; Tang, T.; Li, M.; Liu, M. Designing nitrogen and phosphorus co-doped graphene quantum dots/g-C<sub>3</sub>N<sub>4</sub> heterojunction composites to enhance visible and ultraviolet photocatalytic activity. *Appl. Surf. Sci.* **2021**, *548*, 149211. [[CrossRef](#)]
18. Li, F.; Li, M.; Luo, Y.; Li, M.; Li, X.Y.; Zhang, J.Y.; Wang, L. The synergistic effect of pyridinic nitrogen and graphitic nitrogen of nitrogen-doped graphene quantum dots for enhanced TiO<sub>2</sub> nanocomposites’ photocatalytic performance. *Catalysts* **2018**, *8*, 438. [[CrossRef](#)]
19. Li, F.; Sun, L.; Luo, Y.; Li, M.; Xu, Y.J.; Hu, G.H.; Li, X.Y.; Wang, L. Effect of thiophene S on the enhanced ORR electrocatalytic performance of sulfur-doped graphene quantum dot/reduced graphene oxide nanocomposites. *RSC Adv.* **2018**, *8*, 19635–19641. [[CrossRef](#)]
20. Ghaffarkhah, A.; Hosseini, E.; Kamkar, M.; Sehat, A.A.; Dordanihaghighi, S.; Allahbakhsh, A.; van der Kuur, C.; Arjmand, M. Synthesis, applications, and prospects of graphene quantum dots: A comprehensive review. *Small* **2022**, *18*, 2102683. [[CrossRef](#)]
21. Gao, P.; Wang, G.; Zhou, L. Luminescent sulfur quantum dots: Synthesis, properties and potential applications. *Chemphotochem* **2020**, *4*, 5235–5244. [[CrossRef](#)]
22. Pal, A.; Arshad, F.; Sk, M.P. Emergence of sulfur quantum dots: Unfolding their synthesis, properties, and applications. *Adv. Colloid Interface Sci.* **2020**, *285*, 102274. [[CrossRef](#)] [[PubMed](#)]
23. Li, S.X.; Chen, D.J.; Zheng, F.Y.; Zhou, H.F.; Jiang, S.X.; Wu, Y.J. Water-soluble and lowly toxic sulphur quantum dots. *Adv. Funct. Mater.* **2014**, *24*, 7133–7138. [[CrossRef](#)]
24. Shen, L.H.; Wang, H.N.; Liu, S.N.; Bai, Z.W.; Zhang, S.C.; Zhang, X.R.; Zhang, C.X. Assembling of sulfur quantum dots in fission of sublimed sulfur. *J. Am. Chem. Soc.* **2018**, *140*, 7878–7884. [[CrossRef](#)]
25. Song, Y.H.; Tan, J.S.; Wang, G.; Gao, P.X.; Lei, J.H.; Zhou, L. Oxygen accelerated scalable synthesis of highly fluorescent sulfur quantum dots. *Chem. Sci.* **2020**, *11*, 772–777. [[CrossRef](#)]

26. Liu, G.; Niu, P.; Yin, L.; Cheng, H.-M. Alpha-sulfur crystals as a visible-light-active photocatalyst. *J. Am. Chem. Soc.* **2012**, *134*, 9070–9073. [[CrossRef](#)]
27. Wu, Z.; Liang, Y.; Yuan, X.; Zou, D.; Fang, J.; Jiang, L.; Zhang, J.; Yang, H.; Xiao, Z. MXene Ti<sub>3</sub>C<sub>2</sub> derived Z-scheme photocatalyst of graphene layers anchored TiO<sub>2</sub>/g-C<sub>3</sub>N<sub>4</sub> for visible light photocatalytic degradation of refractory organic pollutants. *Chem. Eng. J.* **2020**, *394*, 124921. [[CrossRef](#)]
28. Chang, X.; Fan, H.; Lei, L.; Wu, X.; Wang, W.; Ma, L. Generation mechanism of the defects in g-C<sub>3</sub>N<sub>4</sub> synthesized in N<sub>2</sub> atmosphere and the method for improving photocatalysis activity. *Catalysts* **2023**, *13*, 269. [[CrossRef](#)]
29. Dong, G.; Wen, Y.; Fan, H.; Wang, C.; Cheng, Z.; Zhang, M.; Ma, J.; Zhang, S. Graphitic carbon nitride with thermally-induced nitrogen defects: An efficient process to enhance photocatalytic H<sub>2</sub> production performance. *RSC Adv.* **2020**, *10*, 18632–18638. [[CrossRef](#)] [[PubMed](#)]
30. Yang, Q.S.; Hu, S.N.; Yao, Y.X.; Lin, X.G.; Du, H.W.; Yuan, Y.P. Engineering graphitic carbon nitride with expanded interlayer distance for boosting photocatalytic hydrogen evolution. *Chin. J. Catal.* **2021**, *42*, 217–224. [[CrossRef](#)]
31. Sano, T.; Tsutsui, S.; Koike, K.; Hirakawa, T.; Teramoto, Y.; Negishi, N.; Takeuchi, K. Activation of graphitic carbon nitride (g-C<sub>3</sub>N<sub>4</sub>) by alkaline hydrothermal treatment for photocatalytic NO oxidation in gas phase. *J. Mater. Chem. A* **2013**, *1*, 6489. [[CrossRef](#)]
32. Zhang, C.; Qin, D.; Zhou, Y.; Qin, F.; Wang, H.; Wang, W.; Yang, Y.; Zeng, G. Dual optimization approach to Mo single atom dispersed g-C<sub>3</sub>N<sub>4</sub> photocatalyst: Morphology and defect evolution. *Appl. Catal. B* **2022**, *303*, 120904. [[CrossRef](#)]
33. Hu, S.; Ma, L.; Xie, Y.; Li, F.; Fan, Z.; Wang, F.; Wang, Q.; Wang, Y.; Kang, X.; Wu, G. Hydrothermal synthesis of oxygen functionalized S-P codoped g-C<sub>3</sub>N<sub>4</sub> nanorods with outstanding visible light activity under anoxic conditions. *Dalton Trans.* **2015**, *44*, 20889–20897. [[CrossRef](#)] [[PubMed](#)]
34. Bai, X.; Wang, L.; Zong, R.; Zhu, Y. Photocatalytic activity enhanced via g-C<sub>3</sub>N<sub>4</sub> nanoplates to nanorods. *J. Phys. Chem. C* **2013**, *117*, 9952–9961. [[CrossRef](#)]
35. Tang, R.; Gong, D.; Deng, Y.; Xiong, S.; Zheng, J.; Li, L.; Zhou, Z.; Su, L.; Zhao, J. Pi-pi stacking derived from graphene-like biochar/g-C<sub>3</sub>N<sub>4</sub> with tunable band structure for photocatalytic antibiotics degradation via peroxymonosulfate activation. *J. Hazard. Mater.* **2022**, *423*, 126944. [[CrossRef](#)] [[PubMed](#)]
36. Yang, J.; Miao, H.; Li, W.L.; Li, H.Q.; Zhu, Y.F. Designed synthesis of a p-Ag<sub>2</sub>S/n-PDI self-assembled supramolecular heterojunction for enhanced full-spectrum photocatalytic activity. *J. Mater. Chem. A* **2019**, *7*, 6482–6490. [[CrossRef](#)]
37. Gao, Q.; Xu, J.; Wang, Z.; Zhu, Y. Enhanced visible photocatalytic oxidation activity of perylene diimide/g-C<sub>3</sub>N<sub>4</sub> n-n heterojunction via  $\pi$ - $\pi$  interaction and interfacial charge separation. *Appl. Catal. B* **2020**, *271*, 118933. [[CrossRef](#)]
38. Sherpa, S.D.; Paniagua, S.A.; Levitin, G.; Marder, S.R.; Williams, M.D.; Hess, D.W. Photoelectron spectroscopy studies of plasma-fluorinated epitaxial graphene. *J. Vac. Sci. Technol.* **2012**, *30*, 03D102. [[CrossRef](#)]
39. Chen, M.J.; Zhou, H.Q.; Qiu, C.Y.; Yang, H.C.; Yu, F.; Sun, L.F. Layer-dependent fluorination and doping of graphene via plasma treatment. *Nanotechnology* **2012**, *23*, 115706. [[CrossRef](#)]
40. Huang, S.; Yang, E.; Yao, J.; Chu, X.; Liu, Y.; Xiao, Q. Nitrogen, phosphorus and sulfur tri-doped carbon dots are specific and sensitive fluorescent probes for determination of chromium(VI) in water samples and in living cells. *Mikrochim. ACTA* **2019**, *186*, 851. [[CrossRef](#)]
41. Liu, W.; Ning, C.; Sang, R.; Hou, Q.; Ni, Y. Lignin-derived graphene quantum dots from phosphous acid-assisted hydrothermal pretreatment and their application in photocatalysis. *Ind. Crops Prod.* **2021**, *171*, 113963. [[CrossRef](#)]
42. Wang, X.C.; Maeda, K.; Thomas, A.; Takanabe, K.; Xin, G.; Carlsson, J.M.; Domen, K.; Antonietti, M. A metal-free polymeric photocatalyst for hydrogen production from water under visible light. *Nat. Mater.* **2009**, *8*, 76–80. [[CrossRef](#)] [[PubMed](#)]
43. Wang, J.; Wang, G.; Cheng, B.; Yu, J.; Fan, J. Sulfur-doped g-C<sub>3</sub>N<sub>4</sub>/TiO<sub>2</sub> S-scheme heterojunction photocatalyst for congo red photodegradation. *Chin. J. Catal.* **2021**, *42*, 56–68. [[CrossRef](#)]
44. Li, F.; Tang, M.; Li, T.; Zhang, L.; Hu, C. Two-dimensional graphene/g-C<sub>3</sub>N<sub>4</sub> in-plane hybrid heterostructure for enhanced photocatalytic activity with surface-adsorbed pollutants assistant. *Appl. Catal. B* **2020**, *268*, 118397. [[CrossRef](#)]
45. Cui, L.F.; Song, J.L.; McGuire, A.F.; Kang, S.F.; Fang, X.Y.; Wang, J.J.; Yin, C.C.; Li, X.; Wang, Y.G.; Cui, B.X. Constructing highly uniform onion-ring-like graphitic carbon nitride for efficient visible-light-driven photocatalytic hydrogen evolution. *ACS Nano* **2018**, *12*, 5551–5558. [[CrossRef](#)]

**Disclaimer/Publisher's Note:** The statements, opinions and data contained in all publications are solely those of the individual author(s) and contributor(s) and not of MDPI and/or the editor(s). MDPI and/or the editor(s) disclaim responsibility for any injury to people or property resulting from any ideas, methods, instructions or products referred to in the content.